

University of Warwick institutional repository: <http://go.warwick.ac.uk/wrap>

This paper is made available online in accordance with publisher policies. Please scroll down to view the document itself. Please refer to the repository record for this item and our policy information available from the repository home page for further information.

To see the final version of this paper please visit the publisher's website. Access to the published version may require a subscription.

Author(s): H. M. BLACKBURN, S. J. SHERWIN and D. BARKLEY
Article Title: Convective instability and transient growth in steady and pulsatile stenotic flows
Year of publication: 2008
Link to published version:
<http://dx.doi.org/10.1017/S0022112008001717>
Publisher statement: None

Convective instability and transient growth in steady and pulsatile stenotic flows

H. M. BLACKBURN¹,
S. J. SHERWIN² AND D. BARKLEY³

¹Department of Mechanical and Aerospace Engineering, Monash University, Victoria 3800, Australia

²Department of Aeronautics, Imperial College London, SW7 2AZ, UK

³Mathematics Institute and Centre for Scientific Computing, University of Warwick, Coventry CV4 7AL, UK

(Received 21 November 2007 and in revised form 7 April 2008)

We show that suitable initial disturbances to steady or long-period pulsatile flows in a straight tube with an axisymmetric 75%-occlusion stenosis can produce very large transient energy growths. The global optimal disturbances to an initially axisymmetric state found by linear analyses are three-dimensional wave packets that produce localized sinuous convective instability in extended shear layers. In pulsatile flow, initial conditions that trigger the largest disturbances are either initiated at, or advect to, the separating shear layer at the stenosis in phase with peak systolic flow. Movies are available with the online version of the paper.

1. Introduction

Steady and pulsatile flows in straight tubes with smooth axisymmetric contractions (stenoses) are of interest largely since they serve as idealized models of human arterial flows in the presence of atherosclerotic plaque. A number of previous studies have been undertaken of flows in axisymmetric stenotic tubes, both experimental (Khalifa & Giddens 1981; Ojha *et al.* 1989) and computational (Mallinger & Drikakis 2002; Varghese, Frankel & Fischer 2007). These studies demonstrated that the flow could become transitional, if not fully turbulent, at Reynolds numbers relevant to human physiology.

In previous work (Sherwin & Blackburn 2005; Blackburn & Sherwin 2007) stability analysis and direct numerical simulation (DNS) were used to examine asymptotic/long-time global stability of steady and pulsatile flows in an idealized stenotic geometry. The instabilities thus identified give insight into the mechanisms of transition for relatively short-period pulsatile flow: the instabilities are associated with vortex rings blown from the contraction during each pulse. However, it was noted that convective instability may play an important role, particularly for physiologically relevant longer pulse periods, where extended shear layers are often present. While the general behaviour predicted via stability analysis and DNS was in reasonable qualitative agreement with the experiments cited above, those experiments had shown considerable evidence of shear-layer oscillations, a typical form of convective instability. Our DNS also demonstrated the susceptibility of long shear layers, when present, to inflow perturbation. In any real flow and certainly within the human body, inflow noise is always available to trigger shear-layer instabilities, but we have as yet little knowledge of their relative quantitative importance.

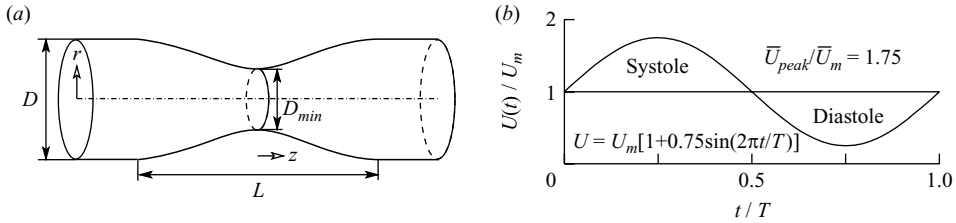


FIGURE 1. (a) Stenosis geometry and (b) pulsatile flow waveform considered in this study.

The emphasis in the present work is on the connection between convective instability and optimal transient growth analysis for these flows when Reynolds numbers are subcritical. Shear flows with streamwise inhomogeneities often exhibit strong convective instability within a localized region. In such cases, the linear response to perturbations is transient: initial growth of a wave packet in the unstable region is followed by decay as perturbations advect into the downstream stable region of the flow. The connection between transient growth and localized convective instability was noted by Cossu & Chomaz (1997), Chomaz (2005), Blackburn, Barkley & Sherwin (2008) and Marquet *et al.* (2008). Here we extend the methodology of Blackburn *et al.* (2008) to unsteady flow.

We consider flows of Newtonian fluid with kinematic viscosity ν in a rigid straight tube, diameter D , with a smooth axisymmetric constriction of co-sinusoidal shape (figure 1a). The relative occlusion is $S = 1 - D_{min}^2/D^2$. In our case, $D_{min}/D = 0.5$, i.e. $S = 0.75$, and the total length of the constriction considered is $L = 2D$. The same geometry has been chosen in a number of previous investigations.

When the inflow is steady, its radial profile some distance upstream of the stenosis is given by the standard parabolic Hagen–Poiseuille solution. When the inflow is pulsatile and periodic, the space–time structure of the radial profile is described analytically as a sum of Bessel–Fourier components (Sexl 1930). As in our previous work, these analytical solutions are used to supply inflow boundary conditions to the base flows. In summarizing the inflows, we employ the instantaneous area-average speed \bar{u} and its time average \bar{u}_m :

$$\bar{u}(t) = \frac{8}{D^2} \int_0^{D/2} u(r, t) r \, dr, \quad \bar{u}_m = \frac{1}{T} \int_0^T \bar{u}(t) \, dt,$$

where $u(r, t)$ is the (axial) velocity and where T is the pulse period; for steady flow, $\bar{u}_m = \bar{u}$. We will use D as a length scale and \bar{u} as a velocity scale, hence the time scale is D/\bar{u} . The key dimensionless parameters of any bulk-flow waveform are its time-average Reynolds number $Re = \bar{u}D/\nu$, the reduced velocity $U_{red} = \bar{u}T/D$, and the peak to mean ratio $\bar{u}_{pm} = \max_{0 \leq t \leq T} \bar{u}(t)/\bar{u}_m = \bar{u}_{peak}/\bar{u}_m$. The reduced velocity gives the number of tube diameters the mean flow travels in a pulse period, but alternatively may be considered as a dimensionless pulse period. We restrict attention to two bulk-flow types: steady flow, and a single-harmonic pulsatile flow with $\bar{u}_{pm} = 1.75$ (see figure 1b), for which

$$\bar{u}(t) = \bar{u}_m \{1 + 0.75 \sin[2\pi(t + t_0)/T]\}, \tag{1.1}$$

where t_0 is an arbitrary time-shift whose use is described in §4. Peak systole and diastole occur for $(t + t_0)/T = 0.25$ and 0.75 , respectively.

For steady inflow, the basic axisymmetric flow contains a jet that expands slowly from the stenotic constriction after separating shortly downstream of the

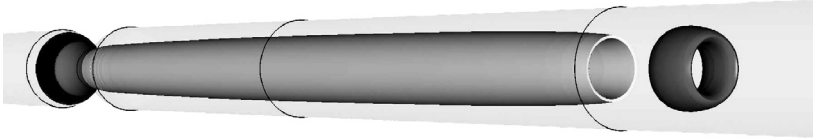


FIGURE 2. Pulsatile stenotic base flow for $U_{red} = 10$, $Re = 400$: snapshot perspective view of separation shear layer (light grey, isosurface of vorticity) extending from stenosis, and its preceding vortex ring (dark grey, isosurface of discriminant of the velocity gradient tensor).

maximum restriction; the jet is surrounded by a long toroidal recirculation zone and axisymmetric shear layer. Steady flow in the present geometry becomes linearly unstable at $Re_c = 722$; the instability mechanism causes a deflection of the jet leading to a weak Coanda-type wall attachment, and occurs with azimuthal wavenumber $k = 1$ (Sherwin & Blackburn 2005).

For simple pulsatile flow with $\bar{u}_{pm} = 1.75$, the primary features of the axisymmetric flow are a vortex ring leading each pulse front, together with an extended shear layer left in the wake of the ring when U_{red} is sufficiently large (figure 2). The vortex ring structures have associated Floquet instabilities, either Widnall-type azimuthal waves ($k > 1$) at short pulse periods, or period-doubling ring-tilting instabilities (with $k = 1$) at longer pulse periods, $U_{red} > 2$ (Blackburn & Sherwin 2007).

When considering pulsatile flow in the present work, we further restrict attention to a case where the dimensionless period is moderately large, $U_{red} = 10$ (e.g. figure 2). The flow has a global instability produced by vortex ring tilting, with $Re_c = 590$. As U_{red} increases, the relative strength of the leading vortex ring decreases, in that a decreasing proportion of the vorticity created on the walls of the contraction during each pulse is contained in the vortex ring. The remainder lies in the extended shear layer, and as can be seen in figure 2, this can be the dominant feature of the flow. Thus as U_{red} rises, the present pulsatile flow arguably becomes increasingly similar in nature to steady flow, since an extended axisymmetric shear layer tends increasingly to be the primary feature.

The largest reduced velocity considered in Blackburn & Sherwin (2007) was also $U_{red} = 10$, but this is tending to the lower limit of what is relevant in the larger vessels of the human arterial tree. For example, in the common carotid artery, typical values of $D = 7.5$ mm, $T = 0.85$ s, $U = 0.25$ m s⁻¹ and $\nu = 4 \times 10^{-6}$ m² s⁻¹ give $U_{red} \approx 28$, while $Re \approx 470$. The fact that this reduced velocity is large compared to that of the flow illustrated in figure 2 strongly suggests that extended shear layers, which may possess localized regions of convective instability, are likely to be an important feature of pulsatile stenotic flow (more generally, separated flow) within parts of the human arterial tree.

In the present paper we apply a time-stepper-based computational methodology for optimal transient growth analysis (Barkley, Blackburn & Sherwin 2008) for the first time in stenotic flows, both steady and pulsatile, and observe that very large linear growth in disturbance energy is possible at Reynolds numbers for which the flow is asymptotically stable. Through analysis over the full range of three-dimensional linear modes, we identify precisely the initial disturbances which lead to maximum linear transient growth.

2. Methodology

The methods employed for examining linear asymptotic stability or transient growth of disturbances are based on time-integration of the linearized Navier–Stokes

equations, which for a perturbation flow \mathbf{u}' and kinematic pressure p' in spatial domain Ω are

$$\partial_t \mathbf{u}' = -(\mathbf{U} \cdot \nabla) \mathbf{u}' - (\mathbf{u}' \cdot \nabla) \mathbf{U} - \nabla p' + Re^{-1} \nabla^2 \mathbf{u}' \quad \text{with} \quad \nabla \cdot \mathbf{u}' = 0 \quad \text{in} \quad \Omega. \quad (2.1)$$

Their action on an initial perturbation $\mathbf{u}'(0)$ over time interval τ may be stated as $\mathbf{u}'(\tau) = \mathcal{A}(\tau) \mathbf{u}'(0)$; the asymptotic/large-time behaviour of linear perturbations is exponential and governed by the leading eigenmodes of $\mathcal{A}(\tau)$. In the following, we focus instead on transient growth over finite times.

As is typical (Schmid & Henningson 2001), we define transient growth with respect to the energy norm of the perturbation flow, derived from the L_2 inner product

$$2E(\mathbf{u}') = (\mathbf{u}', \mathbf{u}') \equiv \int_{\Omega} \mathbf{u}' \cdot \mathbf{u}' \, dV,$$

where E is the kinetic energy per unit mass of a perturbation, integrated over the full domain. If the initial perturbation $\mathbf{u}'(0)$ is taken to have unit norm, then the transient energy growth over interval τ is

$$E(\tau)/E(0) = (\mathbf{u}'(\tau), \mathbf{u}'(\tau)) = (\mathcal{A}(\tau) \mathbf{u}'(0), \mathcal{A}(\tau) \mathbf{u}'(0)) = (\mathbf{u}'(0), \mathcal{A}^*(\tau) \mathcal{A}(\tau) \mathbf{u}'(0)),$$

where we introduce $\mathcal{A}^*(\tau)$, the adjoint of the forward evolution operator $\mathcal{A}(\tau)$. The action of $\mathcal{A}^*(\tau)$ is obtained by integrating the adjoint linearized Navier–Stokes equations

$$-\partial_t \mathbf{u}^* = -(\mathbf{U} \cdot \nabla) \mathbf{u}^* + (\nabla \mathbf{U})^T \cdot \mathbf{u}^* - \nabla p^* + Re^{-1} \nabla^2 \mathbf{u}^* \quad \text{with} \quad \nabla \cdot \mathbf{u}^* = 0 \quad \text{in} \quad \Omega, \quad (2.2)$$

backwards over interval τ . The action of the symmetric operator $\mathcal{A}^*(\tau) \mathcal{A}(\tau)$ on \mathbf{u}' is obtained by sequential time integration of $\mathcal{A}(\tau)$ and $\mathcal{A}^*(\tau)$. The optimal perturbation (leading to largest energy growth over τ) is the eigenfunction of $\mathcal{A}^*(\tau) \mathcal{A}(\tau)$ corresponding to the joint operator's dominant eigenvalue, and so we seek the dominant eigenvalues λ_j and eigenmodes \mathbf{v}_j of the problem

$$\mathcal{A}^*(\tau) \mathcal{A}(\tau) \mathbf{v}_j = \lambda_j \mathbf{v}_j.$$

Typically, $G(\tau) = \max(\lambda_j)$ is used to denote the maximum energy growth obtainable at time τ , while the global maximum is denoted by $G_{max} = \max_{\tau} G(\tau)$.

For an open flow, the most straightforward perturbation velocity boundary condition to apply is $\mathbf{u}' = \mathbf{0}$ over the whole boundary for both the forward and adjoint linearized Navier–Stokes equations. Further discussion of our choice of boundary conditions, methodology and implementation of transient growth analysis for non-parallel shear flows is provided in Barkley *et al.* (2008). Other methods, e.g. based on the full eigenspectrum of the linearized Navier–Stokes equations, may also be used to study transient growth in non-parallel open flows (Ehrenstein & Gallaire 2005; Åkervik *et al.* 2007).

Spectral elements are used for spatial discretization of the axisymmetric geometry in the meridional semi-plane, coupled with a Fourier decomposition in azimuth. Details are given in Blackburn & Sherwin (2004). The same numerics are used to compute base flows, and the actions of the forward and adjoint linearized Navier–Stokes operators. As discussed in Blackburn & Sherwin (2007), long domains are required for the numerical linear stability analysis of this flow; the same is true for transient growth analysis, especially for the pulsatile case investigated at $U_{red} = 10$. Figure 3 shows the computational mesh used for the pulsatile simulations, where it can be seen that the inflow and outflow lengths relative to the throat of the stenosis are respectively $10D$ and $45D$. Mesh structure near the throat is similar to that in

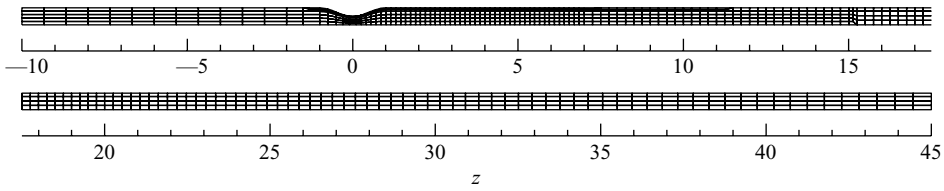


FIGURE 3. Computational mesh in the meridional semi-plane for a cylindrical-coordinate discretization of the geometry, with 949 spectral elements. Overall domain length $55D$.

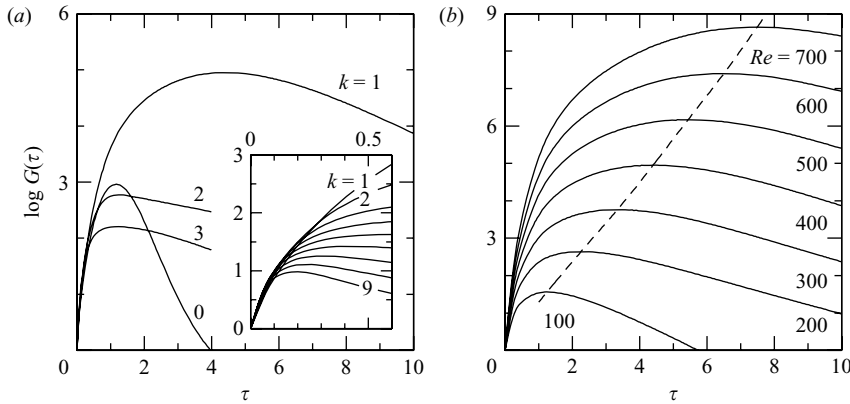


FIGURE 4. Optimal transient energy growth envelopes $G(\tau)$ as a function of time interval τ for steady inflow. (a) $Re = 400$, azimuthal wavenumbers $k = 0-3$; global optimum growth $G_{max} = 8.94 \times 10^4$ occurs for $k = 1$, $\tau = 4.40$. Inset: early time behaviour for $k = 1-9$. (b) Envelopes for wavenumber $k = 1$, $Re = 100-700$; the dashed line shows locus of global maxima.

Blackburn & Sherwin (2007). Base flows are pre-computed and stored as data for the transient growth analysis. In the pulsatile case, 192 time-slices were stored and the base flow reconstructed using Fourier interpolation.

The global maximum eigenvalues λ_0 converge to within 0.1% at $Re = 400$ for the spectral element polynomial order $N = 6$ on the mesh of figure 3 and values reported are for $N = 6$. For steady base flows, the optimal initial conditions for transient growth are always found to be highly concentrated around the flow separation in the stenotic throat and for these an inflow length of $5D$ was adopted. As will be discussed in §4, for pulsatile flow, the global maximum transient growth also occurs for initial conditions concentrated around the throat. However, additional transient-growth initial perturbations of interest are located upstream of the throat and so for all pulsatile flows an inflow of $10D$ was adopted. This change in inflow length has no effect on the global maximum eigenvalue for pulsatile flow to within the eigensolution tolerance of 10^{-5} , whereas near the secondary maximum reported in §4, further increasing the inlet length to $12.5D$ changes the computed eigenvalue by approximately a further 1%. Locations of maximum energy for peak growth always lie well upstream of the domain outflow.

3. Transient disturbances to steady flow

Figure 4(a) shows the envelopes of energy growth for optimal disturbances to steady flow at $Re = 400$ as a function of τ and for azimuthal wavenumbers $k = 0$

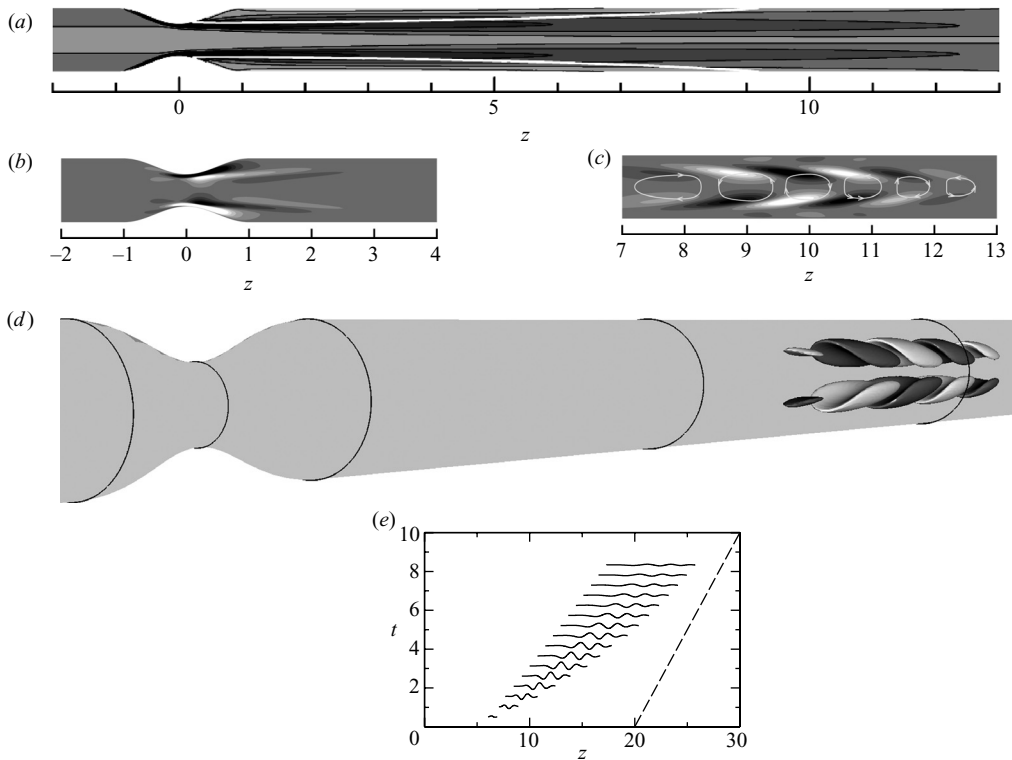


FIGURE 5. An optimal disturbance to steady flow, $Re = 400$. (a) Contours of vorticity in the axisymmetric base flow with separation streamlines. (b) Contours of \pm axial velocity in the optimal perturbation initial condition for azimuthal wavenumber $k=1$, $\tau=4$; (c) of the perturbation at $t=4$ (with sectional streamlines); axial wavelength 1.83. (d) Perspective view of the optimal disturbance represented by \pm isosurfaces of axial velocity component at $\tau=4$, with circumferential lines drawn at $z=-1, 0, 1, 5$ and 10 . (e) Space-time evolution of radial perturbation velocity extracted along $r=0.25$, with the dashed line indicating the mean advection speed of the base flow. The temporal evolution of the optimal disturbance for this case is shown in movie 1.

(axisymmetric) to $k=3$. The first non-axisymmetric wavenumber, $k=1$, provides the largest growth, but as shown by the inset, higher non-axisymmetric modes provide slightly larger growths at small values of τ , similar to transient-growth behaviour for long-wavelength disturbances to steady Hagen–Poiseuille flow (Schmid & Henningson 1994). For $Re = 400$, the global optimum occurs for $\tau = 4.40$ where $G_{max} = 8.94 \times 10^4$. Figure 4(b) shows envelopes $G(\tau)$ for the most-amplified wavenumber $k=1$ for $Re = 100$ – 700 . Global maxima asymptotically grow approximately exponentially with Reynolds number over the examined range while the time interval τ for maximum growth increases approximately linearly with Re . Peak growth for $Re = 700$ is $G_{max} = 4.40 \times 10^8$ at $\tau = 7.49$.

Figure 5 illustrates the characteristics of steady base flows and their optimal disturbances at $Re = 400$. Vorticity contours and separation streamlines of the base flow are shown in figure 5(a). Flow separates almost immediately on encountering the adverse pressure gradient past the throat of the stenosis and remains detached to $z = 9.1$. The axisymmetric shear layer is extended in the axial direction and has minimal curvature in the meridional plane. The optimal growth initial condition for $\tau = 4$, $k = 1$ is illustrated via contours of axial velocity perturbation in figure 5(b).

As for all the optimal disturbances to steady flows, energy in the initial condition is concentrated around the separation line. Figure 5(c) shows contours of optimal axial velocity perturbation at time $t = \tau = 4$, i.e. evolved from the initial condition shown in figure 5(b), together with selected sectional streamlines. The physical nature of the optimal disturbance is more clearly evident in figure 5(d), which shows a perspective view of positive/negative isosurfaces of axial velocity for the optimal disturbance. The perturbation is a wave packet that lies within the axisymmetric shear layer of the base flow, and produces a sinuous disturbance (reflected in the streamlines of figure 5c) that first grows in energy as it advects downstream from its initial location near the flow separation within the throat of the stenosis, reaches maximum energy at $t = \tau$ (when it lies close to the reattachment line at $z = 9.1$), and dissipates as it advects further downstream from its location at the time shown. Figure 5(e) shows a space–time waterfall plot of radial perturbation velocity extracted along the line $r = 0.25$, originating at the throat. We interpret the behaviour as being related to the impulse response wave packet such that the perturbation is initially amplified as it travels through a convectively unstable region, and then decays as it returns to stable Hagen–Poiseuille flow (Blackburn *et al.* 2008; Marquet *et al.* 2008). The temporal evolution of the optimal perturbation for the case illustrated in figure 5 is shown in movie 1 available with the online version of this paper.

4. Transient disturbances to pulsatile flow, $U_{red} = 10$

An additional parameter enters into consideration when the base flow is time-dependent: the phase t_0 at which the disturbance is initiated relative to that of the base flow. This is accommodated simply by time-shifting the base flow, see (1.1). Setting $t_0/T = 0.25$ initiates the disturbance at peak systole, while for $t_0/T = 0.75$ initiation is at peak diastole. We first fix attention on the case where $t_0 = 0$ and carry out a study equivalent to that for steady flow shown in figure 4; the results are summarized in figure 6(a, b). As seen in figure 6(a), perturbations with wavenumber $k = 1$ provide the global maximum. However, as for steady flow, it is found that at very early times, optimal disturbances in higher wavenumbers are slightly favoured over $k = 1$ (inset, figure 6a). Note that while for the pulsatile flow the time-averaged $Re = 400$, the peak systolic value is $Re = 700$, i.e. the maximum employed for the steady-flow computations in § 3.

Having established that perturbations with $k = 1$ are most amplified, we turn to examine the dependence of G on evolution increment τ and initiation phase t_0 , at $Re = 400$, $k = 1$. Figure 6(c) shows example envelopes of optimal growth for different starting phases; $k = 1$, t_0 data from figure 6(a) are included here as the curve emanating from $(\tau + t_0)/T = 0$, with maximum growth achieved near $(\tau + t_0)/T = 1$. In general, there is a distinct bimodal dependence of growth on evolution time, with a pair of local maxima concentrating around $(\tau + t_0)/T = 1$ and $(\tau + t_0)/T = 2$. In order to characterize better the dependence of G on τ and t_0 (at fixed $Re = 400$, $k = 1$), a contour plot of $\log G(\tau, t_0)$ is shown in figure 6(d). The global optimum growth over all evolution times and all initial phases is found to be $G_{max} = 1.10 \times 10^{10}$ – an extremely large value. The initiation phase for the global optimum is approximately $t_0/T = 0.25$, corresponding to initiation near the peak systolic flow, see (1.1). However, in agreement with figure 6(c), figure 6(d) exhibits another local maximum which occurs for initiation at phases near peak diastole ($t_0/T \approx 0.75$), with an approximately eight-magnitude energy growth.

The natures of the pulsatile base flows and the optimal perturbations are illustrated in figure 7. The case first examined (figure 7a–d) is initiated at peak systole

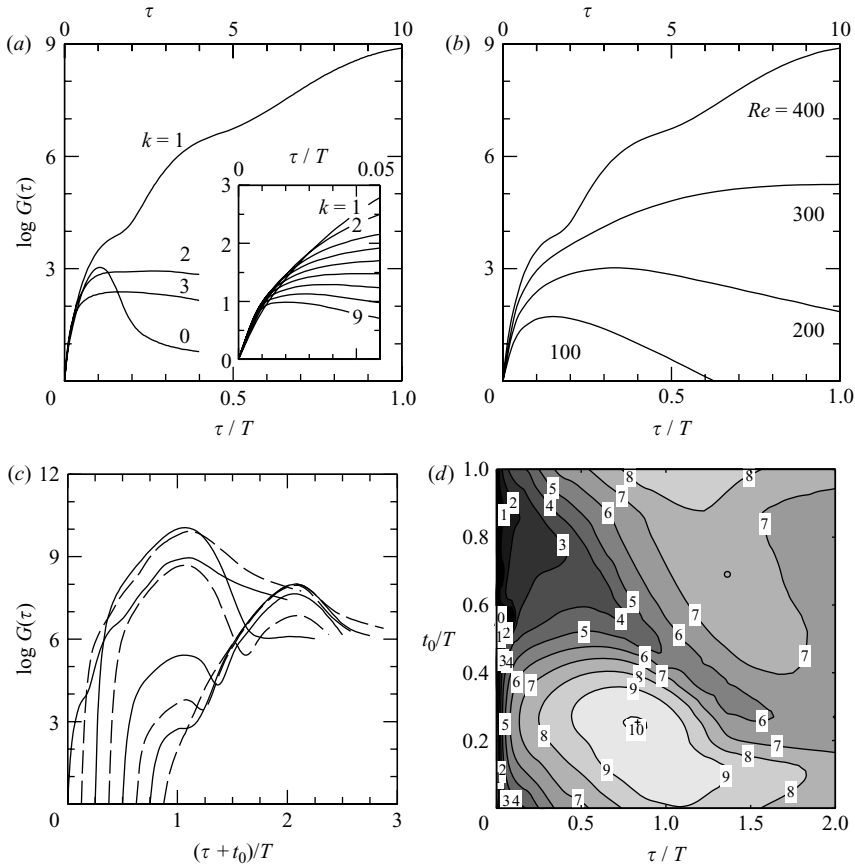


FIGURE 6. Optimal transient energy growth envelopes as a function of relative time for pulsatile inflow with $U_{red} = 10$. (a) $Re = 400$, $t_0 = 0$, with azimuthal wavenumber k as a parameter. (b) $k = 1$, $t_0 = 0$, with Re as parameter. (c) $Re = 400$, $k = 1$, with initiation phase t_0 as parameter. (d) Logarithmic contours of energy growth envelope for $Re = 400$, $k = 1$, as a function of time interval τ and initiation phase t_0 , labelled at decade intervals – the global optimum $G_{max} = 1.10 \times 10^{10}$ at $(\tau/T = 0.83, t_0/T = 0.25)$ is indicated by +, while the secondary maximum, $(\tau/T = 1.36, t_0/T = 0.69)$, $G_{max} = 9.77 \times 10^7$, is indicated by \circ .

($t_0/T = 0.25$) and has growth increment $\tau = 0.875T$, i.e. lies close to the global optimum in parameter space. Figure 7(a) shows vorticity contours of the base flow at peak systole, when the pulse front reaches to approximately $z = 8$; the leading vortex ring lies in the vicinity $z = 7-8$, and it is connected back to the flow separation in the throat by a strong shear layer. In figure 7(c), we can see positive/negative contours of axial velocity in the optimal initial perturbation for the phase point corresponding to figure 7(a). This optimal perturbation is generally similar to that of the steady flow in figure 5(b). Figure 7(b) shows vorticity contours of the base flow at the later time $t = \tau = 0.875T$. By this phase, the original pulse front has progressed to approximately $z = 28$, and a nascent front can be seen at approximately $z = 4.5$. Figure 7(d) shows positive/negative contours of axial velocity in the optimal disturbance outcome at $t = \tau = 0.875T$, i.e. corresponding to the base-flow phase point of figure 7(b), and it is evident that the perturbation resides in the shear layer upstream of the leading pulse front (or vortex ring). As for steady flow, the optimal perturbation is a wave packet which produces a sinuous disturbance to an originally axisymmetric shear layer, that

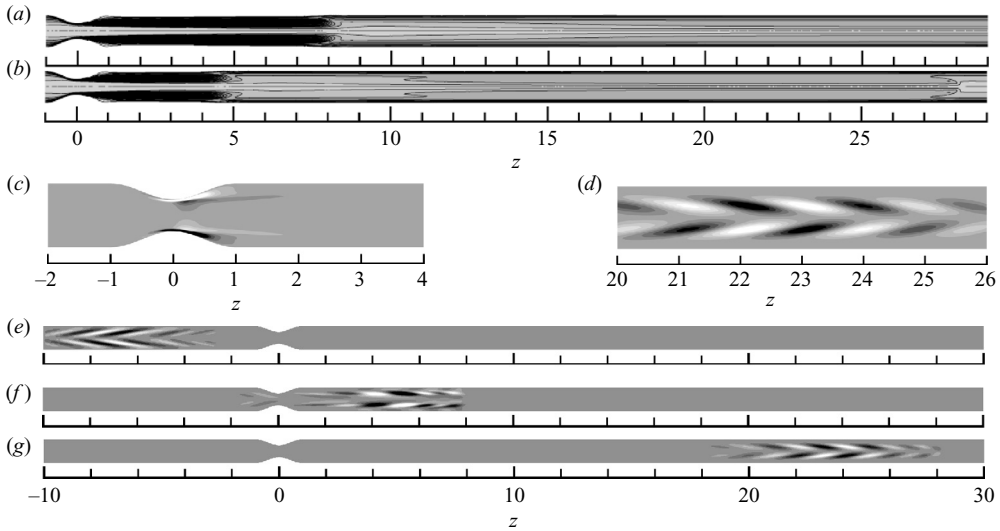


FIGURE 7. Optimal disturbances to pulsatile flow, $U_{red} = 10$, $Re = 400$ with initiation at (a–d) peak systole and (e–g) peak diastole. (a, b) Vorticity contours of base flow for (respectively) $t_0 = 0.25T$, $t = 0$ and $t_0 = 0.25T$, $t = 0.875T$. (c) \pm contours of axial velocity in the optimal disturbance initial condition for $\tau = 0.875T$, when the base flow corresponds to (a); and (d) \pm contours of the resulting perturbation at $t = 0.875T$, when the base flow corresponds to (b). Axial wavelength 1.88. Movie 2 shows the evolution of this case over the interval $0 < t < 0.875T$. (e–g) \pm contours of axial perturbation velocity for the optimal disturbance initiated at peak diastole $t_0/T = 0.75$, and for $\tau/T = 1.375$. The three cases shown are for (e) $t = 0$ (peak diastole), (f) $0.5T$ (peak systole) and (g) $1.375T$. Movie 3 shows more detail of the temporal evolution for this case. Note that the contour levels have been chosen independently for each panel to highlight salient features.

first grows in energy as it advects downstream from near the flow separation, peaks, then dissipates as it advects further downstream. The axial wavelengths of the global optimal disturbances in steady and pulsatile flows are similar, respectively, 1.83 and 1.88. The temporal evolution of the base flow and optimal perturbation for the case illustrated in figure 7(a–d) are shown in movie 2 available with the online version of this paper.

It is also interesting to examine perturbations that lead to the secondary local maximum of figure 6(d), and such a case is examined in figure 7(e–g), which shows axial perturbation velocity contours of the optimal perturbation for ($t_0/T = 0.75$, $\tau/T = 1.375$), leading to an energy growth $G = 9.35 \times 10^7$. In this case, the optimal initial condition resides well upstream of the stenosis throat at diastole, but advects with the base flow in time to arrive at the flow separation line approximately in phase with systole, $0.5T$ later. The subsequent growth mechanism is then similar to that for the global optimum, except that the initial perturbation advects to, rather than being directly initiated at, the stenosis throat at a phase near peak systole. It is clear from the sequence figure 7(e–g) that the optimal perturbation is a wave packet whose axial length scale is closely maintained through the entire process. Note that the axial location for the perturbation at the time of peak growth ($z \approx 23$, figure 7g), is similar to the global optimum (figure 7d). The temporal evolution for this case is shown in movie 3, available with online version.

5. Discussion and conclusions

A central outcome of our analysis is that the peak linear disturbance energy growths in these flows are extremely large. At $Re = 400$, the maximum mean Reynolds number examined for pulsatile flow, the global optimal growth is approximately five orders of magnitude for steady flow and ten orders of magnitude for the pulsatile flow case. Most of this discrepancy in peak energy growth disappears if we consider the characteristic Reynolds number for the pulsatile case to be the peak systolic value ($Re = 700$) rather than the mean, since the peak growth for $Re = 700$ steady base flow is approximately eight and a half orders of magnitude. This possibility is supported by the finding that for pulsatile flow, the temporal phase of the optimal initial disturbance corresponds almost exactly to that of peak systole.

Optimal transient perturbations in both the steady and pulsatile flows examined here have the nature of wave packets whose (similar) axial length scales are preserved through the process of amplification and decay. Since the space–time dynamics of the growth and decay (e.g. figure 5e) mimic those for local convective instability of parallel shear flows and involve axial wave packets, we may infer the presence of a region of convective instability in the flow downstream of the stenosis throat, after which, perturbations decay as they reach a stable region. This convective-type instability occurs at Reynolds numbers well below the critical values for global instability, which are $Re_c = 722$ for steady flow and $Re_c = 590$ for pulsatile flow with $U_{red} = 10$. The global optimal disturbance initial conditions in both cases occur with azimuthal wavenumber $k = 1$, reside in the region of flow separation, and produce sinuous transient motions.

A new physical phenomenon is, however, introduced by the pulsatility, which is associated with the secondary maxima observed in figure 6(c,d). In these cases, the optimal initial condition resides in the flow upstream of the stenosis at pulse phases near diastole, and advects to the separating shear layer in time for peak systolic flow. In practice, this mechanism could be important because it provides a direct path for disturbances in the upstream flow to reach the spatio-temporal region of maximum transient sensitivity (i.e. the separating shear layer at the time of peak systole).

To put the predicted large linear growths into some perspective, we should point out that the introduction of nonlinearity is relatively stabilizing at the Reynolds numbers investigated. This has been established using DNS of both steady and pulsatile flows at $Re = 400$, seeded either with statistically uniform white noise velocity perturbation (at level $|\mathbf{u}'| = 10^{-3}$) or with the optimal-growth initial condition added to the base flow at a relative energy level of 10^{-6} . In all cases, the physical properties of disturbances were similar (e.g. occurred with azimuthal wavenumber $k = 1$, consisted of a sinuous shear-layer disturbance, and arose at similar times) to those predicted linearly. However, the peak energy growths in DNS were somewhat lower than the linear predictions. With increasing initial perturbation level, the perturbation energy growth obtained through DNS falls further below the linear prediction.

Although the geometry considered here is idealized, the results nevertheless have important implications for the flow in real systems, including those in the human arterial tree. The fact that the transient linear responses are so large suggests that energetic local convective instabilities could well be dominant for many *in vivo* stenotic flows.

We are grateful to a referee for suggestions which significantly improved the paper.

REFERENCES

- ÅKERVIK, E., HÖPFFNER, J., EHRENSTEIN, U. & HENNINGSON, D. S. 2007 Optimal growth, model reduction and control in a separated boundary-layer flow using global eigenmodes. *J. Fluid Mech.* **579**, 305–314.
- BARKLEY, D., BLACKBURN, H. M. & SHERWIN, S. J. 2008 Direct optimal growth analysis for timesteppers. *Intl J. Numer. Meth. Fluids* (In press).
- BLACKBURN, H. M. & SHERWIN, S. J. 2004 Formulation of a Galerkin spectral element–Fourier method for three-dimensional incompressible flows in cylindrical geometries. *J. Comput. Phys.* **197** (2), 759–778.
- BLACKBURN, H. M. & SHERWIN, S. J. 2007 Instability modes and transition of pulsatile stenotic flow: pulse-period dependence. *J. Fluid Mech.* **573**, 57–88.
- BLACKBURN, H. M., BARKLEY, D. & SHERWIN, S. J. 2008 Convective instability and transient growth in flow over a backward-facing step. *J. Fluid Mech.* **603**, 271–304.
- CHOMAZ, J.-M. 2005 Global instabilities in spatially developing flows: non-normality and nonlinearity. *Annu. Rev. Fluid Mech.* **37**, 357–392.
- COSSU, C. & CHOMAZ, J. M. 1997 Global measures of local convective instabilities. *Phys. Rev. Lett.* **78**, 4387–4390.
- EHRENSTEIN, U. & GALLAIRE, F. 2005 On two-dimensional temporal modes in spatially evolving open flows: the flat-plate boundary layer. *J. Fluid Mech.* **536**, 209–218.
- KHALIFA, A. M. A. & GIDDENS, D. P. 1981 Characterization and evolution of poststenotic disturbances. *J. Biomech.* **14** (5), 279–296.
- MALLINGER, F. & DRIKAKIS, D. 2002 Instability in three-dimensional, unsteady, stenotic flows. *Intl J. Heat Fluid Flow* **23**, 657–663.
- MARQUET, O., SIPP, D., CHOMAZ, J.-M. & JACQUIN, L. 2008 Amplifier and resonator dynamics of a low-Reynolds-number recirculation bubble in a global framework. *J. Fluid Mech.* **605**, 429–443.
- OJHA, M., COBBOLD, R. S. C., JOHNSTON, K. W. & HUMMEL, R. L. 1989 Pulsatile flow through constricted tubes: an experimental investigation using photochromic tracer methods. *J. Fluid Mech.* **203**, 173–197.
- SCHMID, P. J. & HENNINGSON, D. S. 1994 Optimal energy density growth in Hagen–Poiseuille flow. *J. Fluid Mech.* **277**, 197–225.
- SCHMID, P. J. & HENNINGSON, D. S. 2001 *Stability and Transition in Shear Flows*. Springer.
- SEXL, T. 1930 Über den von E. G. Richardson entdeckten ‘annulareffekt’. *Z. Phys.* **61**, 349–362.
- SHERWIN, S. J. & BLACKBURN, H. M. 2005 Three-dimensional instabilities and transition of steady and pulsatile flows in an axisymmetric stenotic tube. *J. Fluid Mech.* **533**, 297–327.
- VARGHESE, S. S., FRANKEL, S. H. & FISCHER, P. F. 2007 Direct numerical simulation of stenotic flows. Part 2. Pulsatile flow. *J. Fluid Mech.* **582**, 281–315.